

PAPER

[View Article Online](#)
[View Journal](#) | [View Issue](#)Cite this: *Dalton Trans.*, 2021, **50**, 5493Unveiling the role of the lone electron pair in sesquioxides at high pressure: compressibility of β - $\text{Sb}_2\text{O}_3^\dagger$ Juan Angel Sans, ^a Francisco Javier Manjón, ^a André Luis de Jesus Pereira, ^{a,b} Javier Ruiz-Fuertes, ^c Catalin Popescu, ^d Alfonso Muñoz, ^e Plácida Rodríguez-Hernández, ^e Julio Pellicer-Porres,^f Vanesa Paula Cuenca-Gotor, ^a Julia Contreras-García,^g Jordi Ibañez ^h and Virginia Monteseguro ^{c,f}

The structural, vibrational and electronic properties of the compressed β - Sb_2O_3 polymorph, a.k.a. mineral valentinite, have been investigated in a joint experimental and theoretical study up to 23 GPa. The compressibility of the lattice parameters, unit-cell volume and polyhedral unit volume as well as the behaviour of its Raman- and IR-active modes under compression have been interpreted on the basis of *ab initio* theoretical simulations. Valentinite shows an unusual compressibility up to 15 GPa with four different pressure ranges, whose critical pressures are 2, 4, and 10 GPa. The pressure dependence of the main structural units, the lack of soft phonons, and the electronic density charge topology address the changes at those critical pressures to isostructural phase transitions of degree higher than 2. In particular, the transitions at 2 and 4 GPa can be ascribed to the changes in the interaction between the stereochemically-active lone electron pairs of Sb atoms under compression. The changes observed above 10 GPa, characterized by a general softening of several Raman- and IR-active modes, point to a structural instability prior to the 1st-order transition occurring above 15 GPa. Above this pressure, a tentative new high-pressure phase (s.g. *Pcc2*) has been assigned by single-crystal and powder X-ray diffraction measurements.

Received 27th January 2021,

Accepted 9th March 2021

DOI: 10.1039/d1dt00268f

rsc.li/dalton

Introduction

The study of the different polymorphs of group-XV sesquioxides (valence 3+) has triggered the interest of the scientific community in the last few years.^{1–3} Recent studies have predicted the possible structures of their different polymorphs by

the analysis of their dynamical stability. Thus, their structures can be understood on the basis of deformations of the original defective-fluorite structure^{4,5} by applying a vacant array along different crystallographic directions.

The different polymorphs of these sesquioxides are likely related to the distortion of the charge density produced by the cationic lone electron pair (LEP), belonging to the outer ns^2 electrons, when there is a strong s-p hybridization between the cation and the anion.^{6–8} However, despite the efforts that the scientific community has made to understand the structural stability and formation of the different polymorphs and new phases of these sesquioxides,⁹ the exact role played by the cationic LEP in the different polymorphs remains an open question. It is known that when the distortions are strong enough, the LEP effect can force the structures to form closed-molecular units separated from each other. This is the case of the most symmetric cubic structures of minerals arsenolite ($\text{c-As}_2\text{O}_3$) and senarmontite ($\alpha\text{-Sb}_2\text{O}_3$), where the large influence of the LEP stabilizes a structure with a large number of voids. The behaviour of arsenolite and senarmontite has been recently studied under compression.^{10–14} While arsenolite shows no pressure-induced transition, a high-pressure (HP) phase of senarmontite has been recently elucidated and

^aInstituto de Diseño para la Fabricación y Producción Automatizada, MALTA Consolider Team, Universitat Politècnica de València, 46022 València, Spain.

E-mail: juasant2@upv.es

^bLaboratório de Plasmas e Processos (LPP), Instituto Tecnológico de Aeronáutica (ITA), 12228-900, São José dos Campos, Brazil

^cDCITIMAC, MALTA Consolider Team, Universidad de Cantabria, Santander 39005, Spain

^dALBA-CELLS, 08290 Cerdanyola del Vallès, Barcelona, Spain

^eDepartamento de Física, Instituto de Materiales y Nanotecnología, MALTA Consolider Team, Universidad de La Laguna, 38207 San Cristóbal de La Laguna, Spain

^fDepartamento de Física Aplicada-ICMUV, MALTA-Consolider Team, Universitat de València, València, Spain

^gCNRS, UMR 7616, Laboratoire de Chimie Théorique, F-75005 Paris, France

^hGeosciences Barcelona (GEO3BCN-CSIC), 08028 Barcelona, Spain

[†]Electronic supplementary information (ESI) available. CCDC 2044072. For ESI and crystallographic data in CIF or other electronic format see DOI: 10.1039/d1dt00268f

labelled alpha-II [space group (s.g.) 114, $P4_21c$, $Z = 4$], being structurally quite similar to tetragonal $\beta\text{-Bi}_2\text{O}_3$.¹⁴

The less symmetric structures of group-XV sesquioxides and the behaviour of the cationic LEP in these compounds have also been studied at HP. In particular, the polymorphs belonging to the monoclinic symmetry $\alpha\text{-Bi}_2\text{O}_3$ ($\beta\text{-As}_2\text{O}_3$), a.k.a. mineral bismite (claudetite I) have shown a large structural stability at HP up to 20 (40) GPa.^{15,16} A different behaviour has been observed in another monoclinic phase of As_2O_3 , a.k.a. claudetite II, that shows a pressure-induced isostructural phase transition (IPT) above 2 GPa.¹⁷

Finally, sesquioxides with intermediate symmetric structures (tetragonal and orthorhombic), like $\beta\text{-Bi}_2\text{O}_3$, $\varepsilon\text{-Bi}_2\text{O}_3$,¹⁸ and $\beta\text{-Sb}_2\text{O}_3$, are not so well studied at HP although they can be the key structures to understand the cationic LEP activity and its contribution to HP polymorphs. In these latter polymorphs, the LEP effect triggers the formation of empty cavities arranged along a certain crystallographic direction. Among these compounds, only the HP behaviour of $\beta\text{-Bi}_2\text{O}_3$ has been thoroughly studied, giving rise to a 2nd order ferroelastic IPT above 2 GPa caused by an electronic charge redistribution around the BiO_6 polyhedra.¹⁹ Since the cationic LEP stereoactivity is more intense in compounds with smaller unit-cell volumes,²⁰ sesquioxides formed with cations with a smaller ionic radius than Bi (As or Sb) should exhibit a larger influence of the LEP. Thus, the HP study of orthorhombic $\beta\text{-Sb}_2\text{O}_3$ with similar empty linear channels to those of $\beta\text{-Bi}_2\text{O}_3$ can be very interesting to uncover the role played by the LEP in the formation of the different group-XV sesquioxide polymorphs and understand their pressure-induced transformations.

In particular, the Sb_2O_3 compound is used as a retardant in a number of materials,^{21,22} as an oxidation catalyst in several production processes,^{23,24} as an anode material for Li- and Na-ion batteries,^{25,26} to increase stability and decrease wear in fluid lubricants,²⁷ to enhance the properties of glasses,^{28,29} and also as a dopant to modify the conductivity of semiconductors, like SnO_2 and ZnO .^{30–33} Furthermore, the synthesis, properties, and applications of the nanoparticles of antimony oxides have been recently reviewed since they possess excellent properties as compared to bulk materials, like a higher refractive index, absorptivity, abrasive resistance, and proton conductivity.³⁴

In the literature, previous HP Raman scattering (RS)^{35,36} and X-ray diffraction (XRD) studies³⁷ have shown that $\beta\text{-Sb}_2\text{O}_3$ undergoes a structural phase transition above 15 GPa. Although these works have reported the overall compression of valentinite up to 40 GPa, showing the presence of two polymorphs up to that pressure, the behaviour of the low-pressure (LP) phase of $\beta\text{-Sb}_2\text{O}_3$ prior to the structural phase transition to the HP phase, that was proposed to be of monoclinic symmetry, has not been clearly reported.³⁷ This has motivated us to perform a detailed experimental and theoretical study on the structural, vibrational and electronic properties of $\beta\text{-Sb}_2\text{O}_3$ under compression with a thorough analysis of the theoretical electronic charge topology of the LP phase. We will show that compressed valentinite exhibits several internal transitions,

prior to its structural phase transition above 15 GPa. Most of these internal transitions will be shown to be related to the changes in the cationic LEP under compression and could be considered as IPTs of order higher than 2. The incompleteness of Landau and Lifshitz's description of solid phase transitions³⁸ was already stated by Lifshitz in 1960 with the inclusion of the electronic topological transitions (ETTs) as the transitions of order $2^{\frac{1}{2}}$ (higher than 2)³⁹ according to Ehrenfest's notation.⁴⁰ The 2nd order phase transitions require a soft mode, according to Landau's theory; however, the changes observed in this work are associated with the changes in the interaction of the cationic LEPs, *i.e.* of electronic origin, like the one observed in ETTs, which are ascribed to transitions of order higher than 2. Recent studies⁴¹ have proved the existence of IPTs of order higher than 1 (continuous), and some of them are associated with changes in the electronic topology.

Therefore, this work shows the importance of the cationic LEP activity in relation to the rest of the electrons in the molecular unit in order to understand the properties of a quasi-molecular material, like $\beta\text{-Sb}_2\text{O}_3$. Moreover, thanks to the combination of single-crystal and powder XRD measurements, we will propose an orthorhombic HP phase [s.g. $Pcc2$] above 15 GPa which is different from the monoclinic HP phase previously proposed.³⁷ Consequently, this study allows us to understand the polymorphism of group XV sesquioxides and becomes interesting for the future analysis of other LEP-based molecular and quasi-molecular solids under extreme conditions.

Results

Structural properties of $\beta\text{-Sb}_2\text{O}_3$ under compression

The structure of $\beta\text{-Sb}_2\text{O}_3$ [s.g. 56, $Pccn$, $Z = 4$] at room pressure has been traditionally interpreted to be formed by SbO_3E units (see the SbO_3 polyhedral unit in the bottom part of Fig. 1), where E refers to the cationic LEP. The link of different SbO_3E units along the c -axis (two-fold rotation axis) forms rods composed of infinite $(\text{Sb}_2\text{O}_3)_\infty$ chain molecules in such a way that the neighbouring LEPs form empty linear channels parallel to the rods. In this context, $\beta\text{-Sb}_2\text{O}_3$ can be considered as a quasi-molecular solid (with infinite molecules along the c -axis) or as an acicular solid since it grows in the form of $(\text{Sb}_4\text{O}_6)_\infty$ needles extended along the c -axis (see Fig. 1).

Along each rod, each Sb atom is mainly linked to three O atoms forming strong Sb–O bonds of *ca.* 2.0 Å (see the bottom part of Fig. 1); thus, Sb is threefold coordinated at room pressure. As regards the O coordination, the central O atom of each Sb_2O_3 unit along the chain, hereafter named O1, is bonded to the two Sb atoms of the same unit (bond distance of 2.0 Å). Besides, it must be noted that O1 is also weakly bonded to the two Sb atoms (with a bond distance of 2.6 Å) of the neighbouring Sb_2O_3 unit along the infinite chain (see oblique dashed lines in the top right part of Fig. 1). On the other hand, each of the external O atoms of each Sb_2O_3 unit

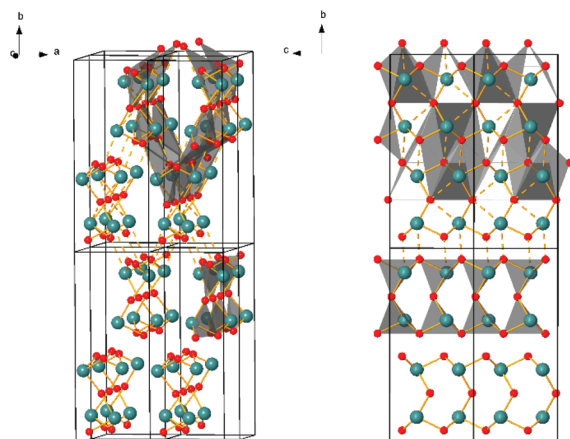


Fig. 1 (Left) 3D structure layout of the low-pressure (LP) phase of β - Sb_2O_3 at ambient pressure (labelling Sb-cyan, O1-red and O2-orange). (Right) Projection of the structure in the b - c plane. Lower parts of the figure show the SbO_3 polyhedral units and two separated chain-like rods within each unit cell extended along the c axis can be observed (LP configuration below 2 GPa). Upper parts of the figure show the SbO_5 polyhedral units so that each rod gets linked with its four neighbor rods (enhanced bonds in the HP configuration above 2 GPa).

along the chain, hereafter named O2, is bonded to an Sb atom of the same unit (with a bond distance of 1.98 Å) and to one Sb atom of the neighbouring Sb_2O_3 unit (with a bond distance of 2.02 Å). In addition, each O2 atom is weakly bonded (a bond distance of 2.5 Å) to an Sb atom in a neighbouring chain (see almost vertical dashed lines in the top part of Fig. 1). This weak bond provides the link between the different chains or rods, leading to the formation of the 3D structure of valentinite. In summary, by considering these weak extra bonds, the structure of valentinite could be interpreted as formed by rods or needles with SbO_5E units, where the coordination of Sb is 3 (with 2 extra-long bonds) and the coordination of O1 and O2 atoms is 2 (with 2 extra-long bonds) and 2 (with 1 extra-long bond), respectively (see the polyhedral SbO_5E unit in the top part of Fig. 1).

Two angle-dispersive powder HP-XRD measurements of β - Sb_2O_3 at room temperature were conducted with two different pressure-transmitting media (PTM). In experiment 1 (2), a 16:3:1 methanol-ethanol-water (MEW) mixture (helium) was used. New reflections, not corresponding to the LP phase of valentinite, were observed only above 15 GPa in both experiments (see Fig. S2 and S3†). This result suggests that the quasi-hydrostatic conditions were maintained up to 15 GPa in both experiments and points to a phase transition above this pressure, in good agreement with the literature.^{35–37} The phase transition is more evident in the case of enhanced quasi-hydrostatic conditions (experiment 2) than in the case of a quasi-hydrostatic environment (experiment 1). A pure HP phase was recorded above 16 GPa in experiment 2, while experiment 1 revealed the coexistence of the LP and HP phases from 16 GPa to 25 GPa. The analysis of the HP phase will be discussed below.

Le Bail analyses (partial Rietveld refinement) of the powder XRD patterns of the LP phase of valentinite in experiment 1 (experiment 2) were carried out up to 14.6 GPa. In the refinement, the atomic coordinates of oxygen were fixed to those obtained by *ab initio* simulations in order to achieve more accuracy in the determination of the coordinates of Sb atoms. An example of the 2D diffraction pattern of experiment 2 and details of the partial Rietveld refinement at selected pressures are shown in Fig. S5 and Table S1.†

The analysis of the LP phase of β - Sb_2O_3 reveals a smooth behaviour in the pressure dependence of the unit-cell volume up to 14.6 GPa (Fig. 2 (left)), without any jump in the volume (associated with a 1st order phase transition) or any apparent change in the compressibility (associated with a 2nd order phase transition). In fact, the data were easily fitted to the 3rd order Birch–Murnaghan (BM) equation of state (EoS) using the EoSFIT software.^{42,43} Interestingly, the unit-cell volumes obtained at similar pressures in both experiments using MEW and helium are almost identical. This result contrasts with the large volume difference observed in arsenolite ($\text{c-As}_2\text{O}_3$) at similar pressures with these two PTM due to the pressure-induced helium trapping in this molecular solid.¹⁰

The bulk modulus obtained for β - Sb_2O_3 in experiment 1 (2) is $B_0 = 24(2)$ GPa ($B_0 = 27.4(8)$ GPa). These values are in good agreement with our theoretical simulations ($B_0 = 30.9(5)$ GPa). The difference between both experiments is likely due to the lack of experimental data below 3 GPa in experiment 2 (due to the helium loading procedure). The agreement between the experiments and calculations supports the validity of our theoretical calculations performed under the GGA-PBESol approximation and will allow us to extend our analysis to different intrinsic properties of this compound. Such a point is crucial because, as we will see below, our simulations show that there are several IPTs of order higher than 2.

The HP dependence of the lattice parameters of β - Sb_2O_3 up to 14.6 GPa (Fig. 2 (right)) exhibits a monotonic sublinear behaviour. Both experimental and theoretical data can be fitted to a modified 2nd order BM EoS (see axial compressibilities and bulk moduli at room pressure in Table S2†). The similarity of data from both experiments suggests that the

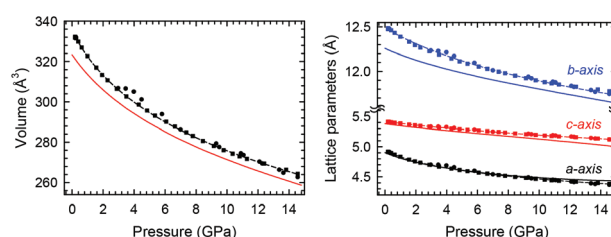


Fig. 2 Pressure dependence of the experimental (symbols) and theoretical (solid lines) unit-cell volume (left) and lattice parameters (right) in β - Sb_2O_3 . Filled squares and empty circles correspond to the data of experiment 1 and experiment 2, respectively. The 3rd order BM EoS fit of the experimental volume data (the dashed line) is also shown. The experimental data fit of the lattice parameters to the modified Murnaghan's EoS (the dashed lines) is also shown.

quasi-hydrostatic conditions are well maintained below 14.6 GPa in both XRD measurements. Consequently, the slight differences between the lattice parameters obtained at LPs in both experiments are likely due to an overpressure of the Cu signal in experiment 2 (in the range between 4 and 6 GPa) since the Cu powder was too close to the gasket. Note that the ratio between the different lattice parameters (Fig. S6†) shows a monotonic variation without any indication of a possible 2nd order IPT up to 14.6 GPa, unlike its counterpart $\beta\text{-Bi}_2\text{O}_3$.^{19,44}

The *c*-axis shows the lowest axial compressibility at room pressure because its pressure behaviour is dominated by the longitudinal compressibility of the rods, mainly related to short Sb–O2 bond distances inside the rods which link different Sb_2O_3 units along the *c*-axis. We can also relate the compressibility of the *c*-axis to the lateral compressibility of the SbO_3E or SbO_5E polyhedral units. The *a*-axis exhibits the highest compressibility because its change is dominated by the compression of the voids between the rods; *i.e.* the compression of the cationic LEPs mainly oriented along the *a*-axis. In any case, a small contribution of the transversal compression of the relatively rigid rods along the *a*-axis cannot be neglected due to the bending of the long Sb–O2 bonds that link the rods mainly directed along the *b*-axis (see almost vertical dashed lines in Fig. 1). Finally, the *b*-axis shows an intermediate compressibility mainly given by the compression of the long Sb–O2 bonds and to a smaller extent by the transversal compression of the rods related to the longitudinal compressibility of SbO_3E (or SbO_5E) units along the *b*-axis. Note that the *b*-axis compressibility is not affected by the compression of the short Sb–O1 bonds (Fig. S9†).

Fig. S7† shows the comparison between our theoretical and experimental (obtained from a partial Rietveld refinement of the HP-XRD patterns) Sb atomic coordinates. These results further confirm that we can rely on the HP evolution of the interatomic distances, polyhedral volume, and compressibilities of the different units obtained from our theoretical calculations. Interestingly, the theoretical pressure dependence of the atomic coordinates of Sb, O1 and O2 atoms shows indications of the anomalous compressibility of valentinite. While some coordinates (Sb_x , Sb_y and O1_z) show a monotonic trend with compression, the rest of the free atomic coordinates, especially those corresponding to external O2 atoms, show a rather different behaviour depending on the pressure range. In particular, the coordinates of O2 reveal three different pressure ranges: (i) from 0 to 4 GPa, (ii) from 4 to 10 GPa and (iii) from 10 to 15 GPa. In addition, the coordinate Sb_z remains almost constant up to 2 GPa and then increases up to 10 GPa, where another slight change in the tendency is observed. In summary, the atomic coordinates of compressed valentinite show structural changes at 2, 4 and 10 GPa which are not detected in the evolution of the unit-cell volume and lattice parameters.

To conclude this section, we will now discuss the nature of the HP phase observed in $\beta\text{-Sb}_2\text{O}_3$ above 14.6 GPa. At this pressure, new reflections appear at 10.8, 12.2, 13.2, and 16 degrees that reflect displacive shifts of some crystallographic planes of the LP phase. We find that the most intense reflec-

tions of the LP phase remain after the phase transition to the HP phase is completed. This result indicates that the HP phase bear a direct relation to the original LP phase. A tentative assignment of the HP phase of valentinite has been performed by comparison with probable structures. The best concordance was achieved with an orthorhombic phase (*s.g.* *Pcc2*, see Fig. S10†). This structure was predicted to be dynamically stable in As_2O_3 ⁵ and is a translationengleiche subgroup of index 2 of *s.g.* *Pccn* of $\beta\text{-Sb}_2\text{O}_3$. In order to corroborate this assignment, we have performed single-crystal HP-XRD measurements of mineral valentinite (Fig. S11†) and *ab initio* theoretical simulations of the proposed HP phase.

In order to understand the results of the single-crystal HP-XRD, we have to bear in mind that the structure of $\beta\text{-Sb}_2\text{O}_3$ at room conditions, with voids extending along the (001) direction, endows the compound with a laminar character and a tendency to exfoliate along the (100) plane. This tendency to exfoliate would be avoided if we could obtain a perfectly oriented (100) single crystal; however, the mineral nature of this sample makes it very difficult to obtain a pure (100) $\beta\text{-Sb}_2\text{O}_3$ single crystal, increasing the probability to form deformations in its crystalline structure. Under compression, the reflections at high 2θ angles quickly fade probably as a result of the slide of the planes in our single crystalline sample. This fact leads to a huge increase of the internal reflection values, R_{int} , which is $\sim 30\%$ at 16 GPa, thus preventing a complete structural determination of the HP phase of $\beta\text{-Sb}_2\text{O}_3$. Despite the difficulty in solving the structure at 16 GPa, we have observed that the new structure also shows an orthorhombic symmetry, $a = 4.590(14)$ Å, $b = 11.113(7)$ Å and $c = 4.9730(16)$ Å, very similar to that of the LP phase. The intensities and new reflections that emerge above 16 GPa in the powder XRD experiment cannot be explained with *s.g.* *Pccn*. However, they are readily indexed to non-centrosymmetric *s.g.* *Pcc2*. Both phases can be distinguished by systematic extinctions related to their symmetry elements. In particular, certain conditions for systematic extinctions ($h00$, $l = 2n$; $0k0$, $k = 2n$; $hk0$, $h + k = 2n$) do not apply in *s.g.* *Pcc2*. Unfortunately, the $h00$ reflections are not accessible in our single crystal due to the orientation of the crystal inside the diamond anvil cell. Furthermore, according to the powder diffraction pattern at 19.3 GPa (Fig. S10†), the $0k0$ and the $hk0$ reflections are extremely weak hindering their localization in our single-crystal patterns (Fig. S11†). Despite these limitations, the integration of the reflections from single-crystal XRD measurements using the CrysAlis program⁴⁵ indicates that the structural data of the HP phase are compatible with *s.g.* *Pcc2*.

The strongest support to the structural determination of the HP phase originates from the single-crystal data. Even though the internal R_{int} value is above 30%, SHELXT⁴⁶ directly displays two sites for the Sb atom conforming to a cationic structure almost identical to the LP structure and in perfect agreement with the structural determination by powder XRD. After several refinement iterations of the cationic structure with program SHELXL,⁴⁷ the $R1$ value goes down to a minimum of 35%, but it is not reduced when we introduce the O positions (Table S3†). Such a drawback, which is the result

of the poor R_{int} value, prevents any total structural determination but confirms the structural determination by powder HP-XRD measurements. The two atoms (Sb and O2) that are in $8e$ crystallographic sites in the LP phase split into two crystallographic sites each with $4e$ symmetry in the HP phase and the atom (O1) that is in the $4d$ Wyckoff site in the LP phase splits into a $2b$ and a $2c$ crystallographic site in the HP phase. The determination of four out of the six positions of the HP phase with single-crystal XRD is further validated by our *ab initio* theoretical simulations (Table S3†) that confirm the orthorhombic HP phase of $\beta\text{-Sb}_2\text{O}_3$ as a distortion of its LP phase instead of the monoclinic structure proposed by Zou *et al.*³⁷

Vibrational properties of $\beta\text{-Sb}_2\text{O}_3$ under compression

Raman spectroscopy and infrared (IR) scattering spectroscopy are very sensitive methods. They have more local character (very sensitive to short-range order changes) than XRD measurements and can show changes in the configuration of interatomic bonds that are difficult to detect by XRD technique. Consequently, they might reflect the anomalous compressibility of the LP phase of valentinite already reported. According to group theory, the centrosymmetric orthorhombic phase of $\beta\text{-Sb}_2\text{O}_3$, with the D_{2h} (mmm) point group, should have 60 zone-centre phonon modes belonging to the following irreducible representation: $\Gamma = 7A_g + 7A_u + 7B_{1g} + 7B_{1u} + 8B_{2g} + 8B_{2u} + 8B_{3g} + 8B_{3u}$.⁴⁸ Three of these modes (B_{1u} , B_{2u} , and B_{3u}) correspond to acoustic phonons, while the seven A_u modes are silent. This results in 30 Raman-active (gerade) optical modes ($\Gamma_R = 7A_g + 7B_{1g} + 8B_{2g} + 8B_{3g}$) and 20 IR-active (ungerade) optical modes ($\Gamma_{\text{IR}} = 6B_{1u} + 7B_{2u} + 7B_{3u}$).

The RS spectrum of $\beta\text{-Sb}_2\text{O}_3$ at room pressure is well known^{35,36,49–52} and has been traditionally divided into two different regions separated by a phonon gap: (i) the low-frequency region (from 50 to 400 cm^{-1}) and (ii) the high-frequency region (from 400 to 800 cm^{-1}). The most intense peaks are located in the low-frequency region that is dominated by a peak near 140 cm^{-1} . The vibrational modes of $\beta\text{-Sb}_2\text{O}_3$ above (below) 400 cm^{-1} were assigned to the internal (external) vibrational modes of pyramidal SbO_3 (or SbO_3E) molecules by many authors. On this basis, Cody *et al.*⁴⁹ suggested that the internal modes should be similar in the different crystalline structures of Sb_2O_3 , senarmonite and valentinite, while the external modes should depend on the particular space group of the crystalline structure due to the different arrangement of molecules inside the unit cell of both compounds. Later, Miller and Cody used the molecule $\text{O}_2\text{Sb-O-SbO}_2$ to describe the internal modes of vitreous Sb_2O_3 and assigned the internal vibrational modes of this molecule.⁵⁰ Finally, a better approach to interpret the RS and IR spectra of valentinite has been reported by Voit *et al.*, who used $\text{Sb}_{10}\text{O}_{15}$ units to model the vibrational spectra.⁵² Our calculations do not support the separation of the vibrational modes of valentinite into external and internal modes of the SbO_3 molecules, as suggested in previous works, since all molecules are linked together in a complex double chain structure which forms infinite $(\text{Sb}_2\text{O}_3)_\infty$ chain molecules. Details of the

vibrational modes of valentinite and its associated atomic motions are provided in Fig. S12–S20.†

A classification of the vibrational spectrum of valentinite is provided by the theoretical phonon density of states (Fig. S21†), which allows one to divide it into three main ranges: (i) low-frequency (below 100 cm^{-1}), where the vibrations are dominated by the motion of the Sb cations; (ii) middle-frequency (100–300 cm^{-1}), where the vibrations are associated with the motion between the polyhedral SbO_3 units as a group (both Sb and O atoms move with predominance of the Sb movement below 230 cm^{-1} and of the O motion above 230 cm^{-1}); and (iii) high-frequency (above 300 cm^{-1}), where there are different kinds of mixed bending and stretching vibrations of SbO_3 units which mainly involve the motion of oxygen atoms.

Unpolarized HP-RS measurements of $\beta\text{-Sb}_2\text{O}_3$ were performed up to 20.7 GPa in both the synthetic powders and single crystals of mineral valentinite (see Fig. S16 and S17†). The RS spectra of valentinite at different pressures are in good agreement with previous reports.^{35,36,49–52} New Raman-active mode frequencies are observed above 14 GPa, thus confirming the transition to the HP phase already found by XRD measurements. Unfortunately, the low quality of the RS data above 14 GPa, even from the single-crystal data, does not help to achieve an unambiguous assignment of the HP phase of $\beta\text{-Sb}_2\text{O}_3$.

The pressure dependence of the experimental and theoretical Raman-active modes of the LP phase in valentinite (Fig. 3) shows a rather good agreement with all data, especially above 150 cm^{-1} where the Raman-active modes are more separated. The comparison of the theoretical and experimental frequencies and pressure coefficients of the Raman-active modes in valentinite (see Tables S4 and S5†) has allowed us to assign in a tentative way the symmetry of many observed Raman peaks. Below 150 cm^{-1} , the symmetry assignment of the Raman-active modes is doubtful for most modes due to the overlapping of many theoretical modes. The pressure dependence of the theoretical IR-active and silent mode frequencies is shown in Fig. S24† and their frequencies and pressure coefficients are summarized in Table S6.† The most striking feature of the pressure dependence of the vibrational modes of valentinite is that many modes show a strong non-linear pressure dependence showing changes around 2, 4 and 10 GPa. These changes agree with those observed in the free atomic coordinates of the Wyckoff positions, as already reported.

Discussion

A thorough analysis of the experimental and theoretical volumes of the SbO_5E polyhedral units and of the empty cavities of the LP phase of $\beta\text{-Sb}_2\text{O}_3$ under compression (Fig. 4) shows that the bulk compressibility of valentinite is strongly dominated by the behaviour of its structural voids. The compression of the theoretical empty cavity volume shows a monotonic variation up to 14.6 GPa that fits perfectly to a single 3rd order BM EoS ($B_0 = 16.9(2)$ GPa). In contrast, fitting of the theoretical SbO_5E polyhedron volume as a function of pressure

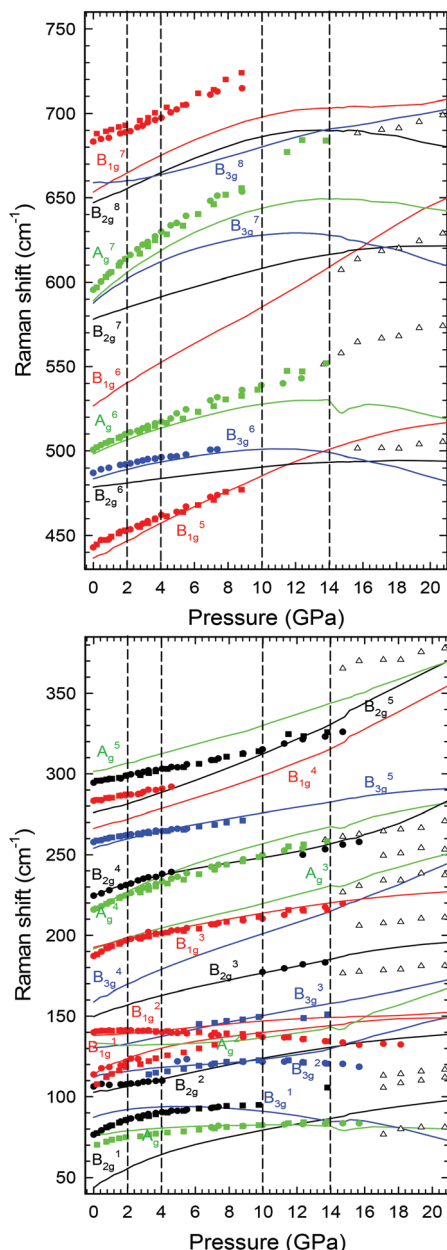


Fig. 3 Pressure dependence of the theoretical (lines) and experimental Raman-active mode frequencies of β - Sb_2O_3 obtained from powder (circles) and single crystals (squares) below 400 cm^{-1} (bottom) and above 400 cm^{-1} (top). Each colour corresponds to an assigned symmetry: green (A_g), red (B_{1g}), black (B_{2g}) and blue (B_{3g}), whose labels are situated near the theoretical curves. The experimental Raman frequencies of the HP phase observed above 15 GPa (empty triangles) are also shown. Vertical dashed lines indicate the pressures at which changes are observed in the Raman mode frequencies.

to a single 3rd order BM EoS in the same pressure range is not possible, thus revealing the existence of two different compressibility regions below and above 2 GPa. Fitting to a 3rd order BM EoS below (above) 2 GPa yields $B_0 = 48(5)$ GPa ($B_0 = 102(10)$ GPa).

Given the existence of 2nd order IPTs in other sesquioxides, like β - Bi_2O_3 , we wonder whether the compressibility changes in

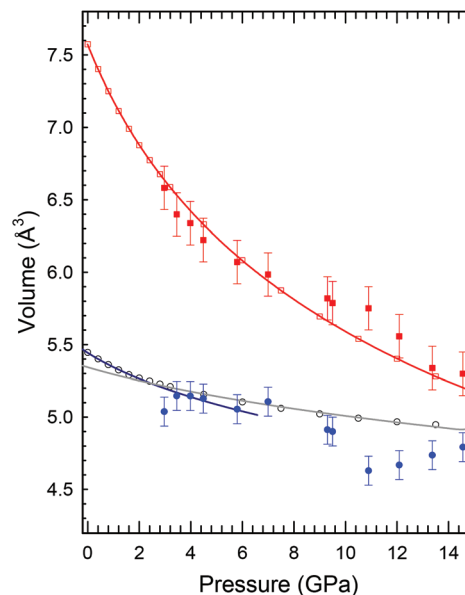


Fig. 4 Pressure dependence of the experimental (solid symbols) and theoretical (empty symbols) volume of the SbO_5E polyhedral unit (blue) and the empty cavity (red) in β - Sb_2O_3 . The 3rd order BM EoS fits (solid lines) of the theoretical data are also shown. Experimental data correspond to experiment 2.

the SbO_5E polyhedron at 2 GPa could be considered as an evidence of a hidden or internal 2nd order IPT. These adjectives indicate that this transition is not reflected in the bulk behaviour, as already analysed, in turn, the transition remains hidden by the strong compressibility of the linear empty cavity that dominates the unit-cell volume compressibility of valentinite.

The F - f plot, F being the reduced pressure and f being the Eulerian strain, is a more sensitive tool than the unit-cell volume vs. pressure plot to observe slight changes in the compressibility.⁴² Therefore, we have analysed the F - f plot for the theoretically simulated bulk structure, polyhedral SbO_5E unit, and the empty cavity under compression (Fig. S8†) in order to achieve a better illustration of the different compressibility ranges of valentinite. The F - f plots have unveiled more than one critical pressure value in the stability pressure range of valentinite. The F - f plot of the bulk structure reveals a compressibility change around 10 GPa which is observed also in the polyhedral unit and the empty cavity. On the other hand, the F - f plot of the polyhedral unit confirms a compressibility change at 2 GPa. Finally, it must be noted that the F - f plot of the empty cavity indicates an additional change around 4 GPa. These pressure values agree with those already found in our study of the lattice dynamics and of the theoretical dependence of free atomic coordinates.

Complementary information about the different compressibility regions of valentinite is provided by the HP behaviour of the Sb–O interatomic distances inside the SbO_5E polyhedral units (Fig. S9†). A strong decrease of the theoretical long Sb–O2 distance (theoretically around 2.42 Å and experimentally around 2.5 Å at 0 GPa) is observed in the range from 0 to 4 GPa. In addition, there is a change in the sign of the slope of

the short Sb–O1 bond in the same pressure range. Note that this is the bond from the central O1 atom to the two Sb atoms of the same Sb_2O_3 molecule. The changes in the Sb–O distances indicate that the main role of pressure up to 2–4 GPa is to bring the neighbouring rods closer, while above this pressure range, the pressure mainly tends to increase the packing inside the rods by compressing the atoms inside the SbO_3 molecular units.

Additional evidence of the extraordinary changes observed at 2, 4, and 10 GPa in valentinite is provided by a detailed comparison of the RS measurements (in single crystals and powders) and theoretical lattice dynamics calculations (Fig. 3 and S22, S23†). At LPs, most experimental Raman-active frequencies show a blueshift with increasing pressure. This is also the case of the most intense Raman peak, located near 140 cm^{-1} at room pressure and tentatively attributed to the B_{1g}^2 mode (Fig. S15†). However, this mode shows a negative pressure coefficient above 2 GPa (Fig. S25†), which agrees with previous HP-RS measurements.^{35,36} In fact, changes in the pressure coefficients of vibrational frequencies around 2 GPa are also observed in other theoretical Raman-active modes (Fig. 3) as well as in IR-active and silent modes (Fig. S24†). In particular, the A_g^2 and B_{3g}^8 modes show a negative (positive) pressure coefficient in $\beta\text{-Sb}_2\text{O}_3$ below (above) 2 GPa.

The changes in the slope of the vibrational frequencies around 4 GPa are experimentally evidenced by the experimental mode near 225 cm^{-1} , assigned to the B_{2g}^4 mode. Note that this mode has a smaller pressure coefficient than the adjacent A_g^4 mode so both modes overlap above 5 GPa and become separated again above 12 GPa (see details in Fig. S26†). Similarly, the theoretical B_{3g}^1 (A_g^2) mode shows a positive (negative) pressure coefficient below (above) 4 GPa, and the contrary occurs above this pressure.

Finally, it must be stressed that many Raman-active modes (A_g^1 , B_{2g}^4 , B_{3g}^6 , B_{3g}^7 , B_{2g}^8 , B_{1g}^7) and IR-active and silent modes show a change in the slope at 10 GPa. In particular, most of these modes show a softening of their frequencies above this pressure, likely related to the increase of the short Sb–O2 bond distance (Fig. S9†). This behaviour suggests the existence of a general instability of the LP phase of $\beta\text{-Sb}_2\text{O}_3$ above 10 GPa (see also the strange kink at theoretical frequencies near 15 GPa). In this regard, we must recall that a complete softening (frequency going down to zero) of a vibrational mode is a signature of a “real” 2nd order phase transition according to the Landau theory of phase transitions, as it occurs in $\beta\text{-Bi}_2\text{O}_3$.^{19,44} In this context, the calculated phonon dispersion curves of $\beta\text{-Sb}_2\text{O}_3$ (Fig. S27†) indicate that there is no complete softening of any vibrational mode along the Brillouin zone in the whole range up to 15 GPa. This result implies that we cannot consider the changes observed in the compressibility of valentinite at 2, 4 and 10 GPa belonging to a 2nd order IPT, so they must be ascribed to the IPTs of order higher than 2.

To conclude the discussion regarding the vibrational properties of valentinite under compression, we must mention that the changes in the compressibility at different pressures have been confirmed not only by the changes in the slopes of the fre-

quencies of vibrational modes, but also by the accurate analysis of the pressure dependence of the full width half-maximum (FWHM) of several high-intensity Raman-active modes, as obtained from the HP-RS measurements on single-crystal samples (Fig. S28†). The HP evolution of the FWHM in two experimental Raman-active modes (one in the low-frequency region and the other in the high-frequency region) shows that the changes in their FWHM occur at roughly the same critical pressures where the changes in the F - f plots are observed. In summary, all HP-RS results experimentally support the conclusions obtained by the analysis of the theoretical simulations regarding the existence of hidden or internal structural changes in valentinite around 2, 4, and 10 GPa. In order to obtain additional evidence for the different ranges of compressibility of valentinite, we have studied the evolution of the topology of the electronic charge distribution by analyzing the atomic Bader volumes and charges in $\beta\text{-Sb}_2\text{O}_3$ (Fig. 5). According to Bader's theory, the change in the topological distribution of the charge around an atom may reveal a variation in the molecular geometry since its electronic distribution should be invariant to pressure.⁵³ The Sb volume and charge show a change in the tendency above 2 and 10 GPa (see deviations from linear trends in Fig. 5) that agrees roughly with the pressure where the compressibility of the SbO_5E polyhedral volume changes. The O2 volume and charge show changes in the tendency between 2 and 4 GPa, which are complementary to that observed in Sb. Finally, the O1 volume and charge follow almost linear trends with a small change in the trend near 2 GPa. These results are consistent with the O1 central position in the rod and suggest that the O1 atoms are barely involved in the compressibility changes observed in valentinite. Consequently, these results show that the anomalous compressibility of the polyhedral SbO_5E unit around 2–4 GPa may be related to a charge transfer between the Sb and O2 atoms. This result clearly indicates that the different rods start to interact in a more intense way above this pressure range. Thus, we can consider that above this pressure range the coordination of the Sb atom reaches a real 3 + 1 coordination with a loss of the isolated rod character at LP; *i.e.* a quasi-1D to a 3D transition occurs between 2 and 4 GPa in valentinite. Therefore, the changes between 2 and 4 GPa could be considered to be related to the internal or hidden 2nd order IPTs not reflected in the bulk compressibility of $\beta\text{-Sb}_2\text{O}_3$. It is noteworthy that a 2nd order IPT has also been observed in $\beta\text{-Sb}_2\text{O}_3$ ^{19,44} and also in Sb_2Te_3 ⁵⁴ and BiMn_2O_5 ,⁵⁵ where the 2nd order IPT was also revealed by the analysis of the evolution of the Bader charge under compression.

Further evidence of the occurrence of subtle compressibility changes in valentinite under compression originates from the analysis of the pressure dependence of the orientation and distortion of the cationic LEPs, which has been studied by the topology of the electronic localization function (ELF). The pressure dependence of the LEP orientation, given by the angle formed by the interacting LEPs and its common bond critical point (BCP), shows a drastic change at 2 GPa (Fig. 6). The change in the orientation of the LEPs around 2 GPa is in good agreement with the features observed in the analysis of

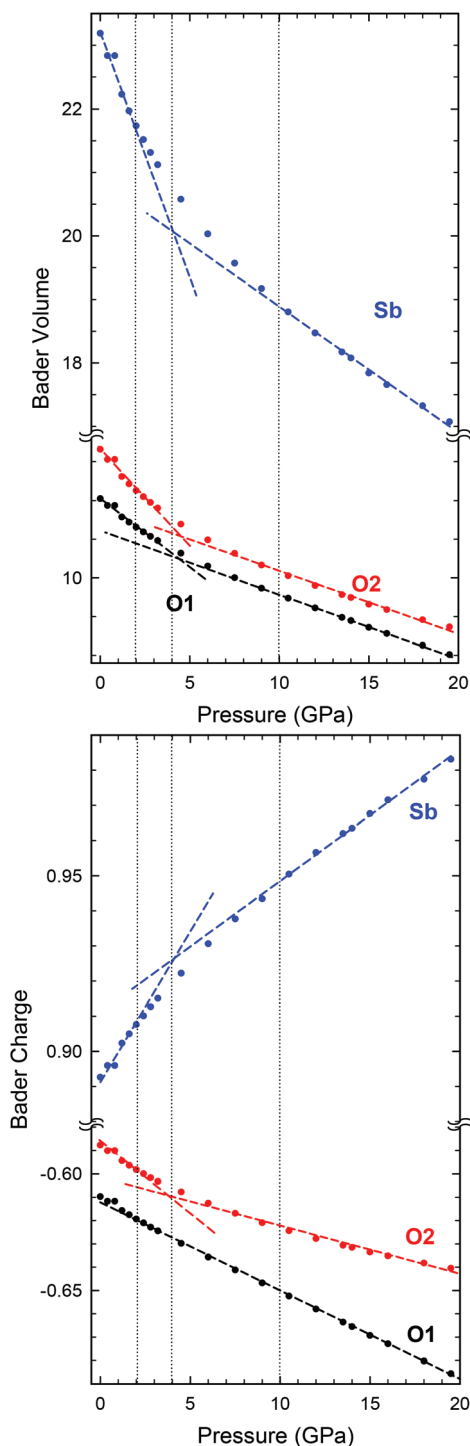


Fig. 5 Evolution of the theoretical Bader volumes (top) and charges (bottom) of the non-equivalent atoms in β - Sb_2O_3 . Dashed straight lines are a guide to the eye in order to help visualize the different tendencies observed.

the atomic Bader volumes and charges and with those observed in the structural and vibrational properties of valentinite. Therefore, we can conclude that the anomalous behaviour of valentinite at 2 GPa is caused by a sudden reorientation

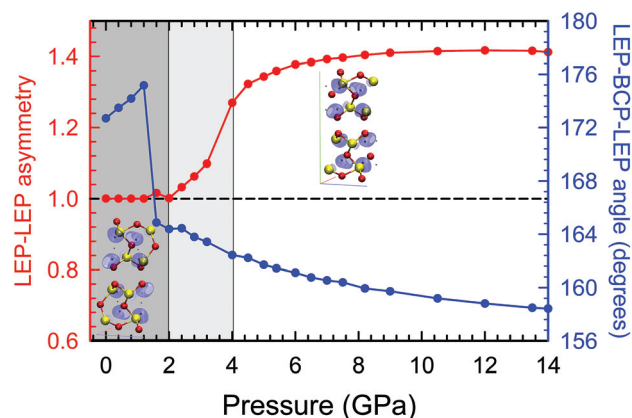


Fig. 6 Evolution of the LEP–LEP asymmetry (red) and the angle formed by neighboring LEPs and the BCP (blue) under compression. The location of the BCP in the structure is displayed in the inset of the figure for each pressure range proposed.

of the cationic LEPs that form the structural voids or channels in valentinite. At room pressure, the LEPs are oriented towards the centre of the empty cavity so they interact with their neighbouring LEPs belonging to different a - c crystallographic planes. The strong compression of the empty cavity along the a -axis (shown by the great decrease of the inter-rod bond distances) shortens the distance between the neighbouring LEPs belonging to the same a - c crystallographic plane in such a way that these LEPs start to interact. This leads to an abrupt change in the LEP–BCP–LEP angle near 2 GPa.

On the other hand, the LEP–LEP asymmetry, measuring the distortion of the two LEP–BCP distances (Fig. 6), indicates a negligible distance asymmetry between the two interacting LEPs below 2 GPa. This asymmetry increases above 2 GPa up to around 4 GPa when it becomes constant. This behaviour can be explained by the great decrease of the void volume and the great reduction of the long interatomic Sb–O2 distances at LPs. Up to 2 GPa, the cationic LEPs suffer from a gradual reorientation remaining barely undistorted; the relative asymmetry with respect to the room pressure value is 1 (no asymmetry). Above 2 GPa, the strong compression between the neighbouring rods causes a sudden reorientation of the cationic LEPs and the effect of pressure begins to distort the cationic LEPs themselves. This distortion is reflected in the increase of the relative asymmetry of the LEP–BCP distances (deviation with respect to 1 that corresponds to the same LEP–BCP distance in the two interacting LEPs). This means that the distortion of the LEP cloud is larger for one LEP than that for its neighbouring one. The difference in the LEP distortions reaches a maximum near 4 GPa; *i.e.*, the LEP cloud considered as an ellipsoid becomes more and more stretched up to 4 GPa. Above this pressure, the LEP cloud cannot be further compressed and the relative LEP asymmetry remains constant. This means that the effect of pressure above 4 GPa is reflected in the decrease of the long interatomic Sb–O distances and especially in the decrease of the second shortest Sb–O2 dis-

tance (Fig. S9†). The compression of the internal Sb–O1 bonds above 4 GPa indicates that a real 3D behaviour is observed above this pressure.

The anomalous hidden or internal behaviours at 2 and 4 GPa cannot be interpreted as pure 2nd order IPTs due to the lack of discontinuities in the thermodynamic parameters, which avoids their assignment in Ehrenfest's classification.⁵⁶ New and extended definitions of phase transitions given by Ma and Wang⁵⁷ introduce type-I transitions. Such a type of transition only requires two stable states without variable discontinuity requirement and is called continuous transition. Unfortunately, the definition of a different initial and final stable state is quite difficult to identify in our case. Another point is that by definition a phase transition shows changes in the atomic bonds (coordination, symmetry or arrangement); however, to our knowledge, the changes in the interaction between unpaired electrons, like LEPs, in inorganic solids under compression, have never been studied. In valentinite, the different interactions between the neighbouring LEPs may cause subtle changes in the properties of valentinite. However, these changes cannot be assigned to a 2nd order IPT in Ehrenfest's classification and consequently should be attributed to a transition of order higher than 2.

Finally, we would like to mention that all F - f plots (Fig. S8†) show a tendency change at 10 GPa, in perfect correlation with a general softening of many vibrational modes (Fig. 3 and S24†). A response to compression is not observed in the analysis of the electronic topology around 10 GPa. As already mentioned, the general softening of the Raman-active and IR-active modes observed above 10 GPa may be the result of an ongoing instability, probably the onset of the phase transition experimentally observed above 15 GPa. However, our *ab initio* calculations do not show any complete softening of the theoretical vibrational modes up to 14 GPa. Note that the B_{2u}^1 mode near 25 cm⁻¹ at room pressure shows an almost complete freezing near 15 GPa. This indicates that the structure becomes fully unstable above 14 GPa when the transition occurs. For this reason, the existence of an electronic-driven IPT around 10 GPa has also been considered. Our theoretical calculations of the electronic band structure at several pressures (Fig. S29†) show a progressive decrease of the bandgap of valentinite. However, neither a change from semiconducting-to-metallic nor a change in the topology of the Fermi level around 10 GPa have been observed. Consequently, the origin of the instability occurring above 10 GPa in valentinite is still unknown and will deserve further studies. In any case, the theoretical interatomic distances in Fig. S9† allow an interesting reading. If we hypothesise that the 3 + 1 coordination of Sb starts at 2 GPa (when the large Sb–O2 distance decreases below 2.36 Å) the increase in the coordination to 3 + 1 + 1 of Sb would start above 10 GPa (when the much larger Sb–O1 distance decreases below 2.38 Å). Moreover, there is a change in the theoretical slope of the two shortest Sb–O2 bond distances above 10 GPa (Fig. S9†). The shortest one shows a reduction of the slope while the largest one shows an increase of the slope; *i.e.* it enlarges at a higher rate which suggests a structural instability.

Consequently, the increase of the coordination of Sb above 10 GPa, thanks to the interaction of the central parts of the neighbouring Sb₂O₃ units in the same rod (involving large Sb–O1 bonds), leads to unusual changes in the Sb–O2 distance and could lead to the instability of the structure of valentinite. In the HP phase, the polyhedral unit shows a five-fold coordination confirming the trend observed with compression. In summary, our analysis shows that the anomalous compressibility of valentinite at 2 and 4 GPa is related to the changes in the cationic LEPs that affect the connectivity of external O2 atoms, while that occurring at 10 GPa is not related to the cationic LEPs but likely related to the changes in the connectivity of internal O1 atoms which in turn affect in a strange way the compressibility of the Sb–O2 bonds.

Experimental

Experimental details

Synthetic 99.9% pure white powders of the β -Sb₂O₃ samples used in the present experiments were acquired from Sigma-Aldrich Inc., while fully transparent single crystals of valentinite were obtained from Lac Nicolet Mine in Quebec (Canada). Angle-dispersive powder HP-XRD measurements at room temperature up to 25 GPa were conducted in a membrane-type diamond anvil cell (DAC) at the BL04-MSPD beamline of ALBA synchrotron in two different experiments. The sample was loaded inside the DAC using either a MEW mixture (experiment 1) or helium (experiment 2) as a PTM. The pressure inside the cavity was calibrated through the EoS of copper.⁵⁸ Incident monochromatic beam at a wavelength of 0.4246 Å was focused at 20 × 20 μm² and cleaned using a pinhole of 50 μm.⁵⁹ Images covering a 2θ range up to 20° were collected using a SX165 CCD located at 240 mm from the sample. Integrated XRD pattern profiles as a function of 2θ were obtained with the Fit2D software.⁶⁰ Le Bail analysis (partial Rietveld refinement) of the experimental diffraction patterns corresponding to experiment 1 (experiment 2) was carried out with the GSAS package software.^{61,62} Partial Rietveld refinement was performed by fitting the atomic coordinates of Sb and fixing the atomic coordinates of O1 and O2 to those obtained by *ab initio* simulations corresponding to each pressure, in order to obtain a better fit of the atomic coordinates of Sb atoms (see Fig. S7 and Table S1†). This procedure was performed because lighter elements are more sensitive to errors in their determination by XRD measurements. Small variations of the free Wyckoff sites may lead to strong changes in the interatomic distances, which can avoid an adequate precision for the experimental determination of bond lengths. The background of each XRD powder pattern was fitted to a shifted Chebyshev function of the 1st kind and the peak shape was analysed using the profile coefficients for Simpson's rule integration of the pseudovoigt function implemented in the GSAS package.

In the single crystal XRD experiment a (100)-oriented single crystal was loaded into a Merrill-Bassett diamond-anvil cell,

equipped with 500 μm culet diamonds. The sample with a surface area of $150 \times 40 \mu\text{m}^2$ was loaded in the pressure chamber made in the 200 μm hole of a tungsten gasket that has been preindented to 80 μm in thickness. The pressure transmitting medium was He and a ruby chip was included for pressure determination. The XRD data were collected at the Beamline I19, at Diamond Light Source, using a Newport kappa-geometry 4-circle diffractometer fitted with a Dectris Pilatus 300 K pixel-array photon-counting detector. The dataset was collected at a wavelength of $\lambda = 0.4895 \text{ \AA}$, with a step size and exposure time of 0.2° and 0.4 seconds, respectively. The data were collected using a series of ω scans to give the optimal completeness when using a diamond anvil cell. The data were integrated with the program CrysAlisPro⁴⁵ which incorporates routines that omit the regions of the detector shaded by the diamond-anvil cell from integration.

Room-temperature unpolarized HP-RS measurements on the powder (up to 22 GPa) and single crystal $\beta\text{-Sb}_2\text{O}_3$ (up to 15 GPa) samples, using MEW as a PTM, were carried out with a Horiba Jobin Yvon LabRAM HR spectrometer equipped with a thermoelectrically cooled multichannel CCD detector that enables a spectral resolution better than 2 cm^{-1} .⁶³ RS measurements were performed using the 6328 \AA line of a He:Ne laser. Special attention was paid to the experimental measurements to avoid the undesired laser heating effects already observed in the cubic polymorph of antimony oxide.⁶⁴ The ruby fluorescence scale⁶⁵ was used to determine the pressure. It must be noted that MEW and helium provide nearly hydrostatic conditions up to 10 GPa and 20 GPa, respectively, and quasi-hydrostatic conditions up to the maximum pressure attained in our experiments.^{66,67}

Theoretical details

Ab initio total-energy calculations were performed for $\beta\text{-Sb}_2\text{O}_3$ within density functional theory (DFT)⁶⁸ using the plane-wave method and pseudopotential theory with the Vienna *Ab initio* Simulation Package (VASP).⁶⁹ The projector-augmented wave scheme (PAW)^{70–73} was employed and the basis set of plane waves was extended up to an energy cutoff of 520 eV in order to achieve highly converged results and the accurate description of the electronic properties. The exchange–correlation energy was taken in the generalized gradient approximation (GGA) with the PBEsol⁷⁴ prescription. To ensure a high convergence of 1–2 meV per formula-unit in the total energy and an accurate computation of the forces on the atoms, the integrations over the Brillouin zone (BZ) were performed using dense meshes of special k -points. At selected volumes, the structure was fully relaxed to the optimized configuration through the calculation of the forces on atoms and the stress tensor. In the optimized configurations, the forces on the atoms were less than $0.002 \text{ eV \AA}^{-1}$ and the deviations of the stress tensor from a diagonal hydrostatic form were smaller than 1 kbar (0.1 GPa). The set of energies E , volumes (V) and pressures (P) obtained was fitted with an equation of state (EoS) to obtain the bulk modulus and its pressure derivative.

The interatomic distances were obtained with the VESTA software.⁷⁵

Lattice-dynamic calculations of the phonon modes were carried out at the zone centre (Γ point) of the BZ with the direct force-constant approach (or the supercell method).⁷⁶ These calculations provide not only the frequency of the normal modes, but also their symmetry and their polarization vectors. This allowed us to identify the irreducible representations and the character of the phonon modes at the Γ -point.

Conclusions

In this experimental and theoretical study of the behaviour under compression of the $\beta\text{-Sb}_2\text{O}_3$ compound, we have confirmed the 1st order phase transition above 15 GPa reported in previous works and have proposed that the HP phase of valentinite has an orthorhombic symmetry (s.g. *Pcc2*) that is a low-symmetry modification of the valentinite structure. The proposed HP phase is supported by *ab initio* simulations, with good quality factors in the analysis of the powder XRD and with its cationic structure confirmed by single crystal XRD.

Thanks to the analysis of the pressure dependence of the Raman-active mode frequencies in valentinite and its comparison with *ab initio* calculations, this work provides a solution to the misunderstanding about the irreducible representation of the vibrational modes of $\beta\text{-Sb}_2\text{O}_3$ found in the literature. Moreover, we have reported a tentative assignment of the symmetry of the observed first-order Raman-active modes of $\beta\text{-Sb}_2\text{O}_3$.

A deep analysis of the compressibility of the theoretically simulated SbO_5E polyhedral unit, the empty linear cavities, and the unit cell volume (F - f plots), as well as the pressure dependence of Sb and O free atomic coordinates reveals changes around 2, 4 and 10 GPa which correlate with the changes observed in the vibrational modes of valentinite under compression. These changes were mainly observed in the HP behaviour of the Bader charge and volume around Sb and O2 and they have been interpreted as changes in the orientation and distortion of cationic LEPs, respectively. In particular, the changes observed at 2 and 4 GPa can be considered as internal IPTs in valentinite, which are hidden (not evidenced in the bulk compressibility) due to the dominance of the compressibility of the voids of the structure in the bulk compressibility. The transitions at 2 and 4 GPa have been identified with an order higher than 2 because they involve a change in the interaction between the neighbouring LEPs (unpaired electrons). These transitions trigger the formation of new bonds, thus increasing the Sb coordination changes from 3 at room pressure to $3 + 1$ above 2 GPa. Hence, they constitute a sequence of transitions from an acicular quasi-molecular solid to a 3D solid.

Finally, the F - f plots show a change in the compressibility of the whole rod-like structure above 10 GPa which is consistent with the general softening of the vibrational modes. We have interpreted this instability to be caused by the strong

interaction between the central O1 atoms and Sb atoms of neighbouring Sb₂O₃ units when the large Sb–O1 distance decreases below 2.38 Å; this leads to an increase in the coordination of Sb atoms to 3 + 1 + 1 above 10 GPa. Therefore, the coordination of Sb clearly increases to 5 in the high-pressure phase above 15 GPa.

We hope that this work will promote further studies on valentinite for an unambiguous identification of the cause of the changes observed above 10 GPa and the determination of its high pressure phase. We also hope that this work, unveiling the interaction between the cationic LEPs in valentinite at 2 GPa, will stimulate further studies on subtle pressure-induced phase transitions in molecular and quasi-molecular solids, especially in compounds with cations featuring stereochemically active LEPs, like in group-XV sesquioxides, where a detailed search could lead to the discovery of new and hitherto unexpected internal transitions.

Author contributions

Conceptualization has been performed by JAS. Writing has been performed by JAS and FJM. Investigation into experimental methods was conducted by JAS, FJM, JR, CP, JP, VPCG, JI and VM. Investigation into theoretical calculations was done by AM, PRH, JCG and VM. Methodology was discussed by JAS and FJM.

Conflicts of interest

There are no conflicts to declare.

Acknowledgements

This research was partially supported by the MINECO (FIS2017-83295-P, MAT2016-75586-C4-1/2/3-P, PGC2018-097520-A-100, RED and PID2019-106383GB-41/42/43), by the MALTA-CONSOLIDER TEAM network (RED2018-102612-T) and by the EU-FEDER. JAS acknowledges the Ramon y Cajal fellowship (RYC-2015-17482) for financial support. VM thanks the Juan de la Cierva Program (FJCI-2016-27291) and Beatriz Galindo Fellowship (BG20/00077) for financial support. We also thank the ALBA (2016091901 experiment) and DIAMOND light source (CY22223 experiment) for providing beamtime, and Mark Warren, Sarah Barnett and Dominik Daisenberger for their help in the single-crystal X-ray diffraction experiment under pressure.

Notes and references

- 1 J. Divya, N. J. Shivaramu, W. D. Roos, W. Purcell and H. C. Swart, Synthesis, surface and photoluminescence properties of Sm³⁺ doped α -Bi₂O₃, *J. Alloys Compd.*, 2021, **854**, 157221.
- 2 K. P. Lakshmi, R. Deivananyagam and M. M. Saijumon, Carbon nanotube 'wired' octahedral Sb₂O₃/graphene aerogel as efficient anode material for sodium and lithium ion batteries, *J. Alloys Compd.*, 2021, **857**, 158267.
- 3 A. F. Gerdelidani, H. Towfighi, K. Shahbazi, D. T. Lamb, G. Choppala, S. Abbasi, A. S. M. Fazle Bari, R. Naidu and M. Mahmudur Rahman, Arsenic geochemistry and mineralogy as a function of particle-size in naturally arsenic-enriched soils, *J. Hazard. Mater.*, 2021, **403**, 123931.
- 4 A. Matsumoto, Y. Koyama and I. Tanaka, Structures and energetics of Bi₂O₃ polymorphs in a defective fluorite family derived by systematic first-principles lattice dynamics calculations, *Phys. Rev. B: Condens. Matter Mater. Phys.*, 2010, **81**, 094117.
- 5 A. Matsumoto, Y. Koyama, A. Togo, M. Choi and I. Tanaka, Electronic structures of dynamically stable As₂O₃, Sb₂O₃, and Bi₂O₃ crystal polymorphs, *Phys. Rev. B: Condens. Matter Mater. Phys.*, 2011, **83**, 214110.
- 6 J. P. Allen, J. J. Carey, A. Walsh, D. O. Scanlon and G. W. Watson, Electronic Structures of Antimony Oxides, *J. Phys. Chem. C*, 2013, **117**, 14759.
- 7 G. W. Watson and S. C. Parker, Origin of the Lone Pair of α -PbO from Density Functional Theory Calculations, *J. Phys. Chem. B*, 1999, **103**, 1258.
- 8 G. W. Watson, S. C. Parker and G. Kresse, Ab initio calculation of the origin of the distortion of α -PbO, *Phys. Rev. B: Condens. Matter Mater. Phys.*, 1999, **59**, 8481.
- 9 Q. Guo, Y. Zhao, C. Jiang, W. L. Mao, Z. Wang, J. Zhang and Y. Wang, Pressure-Induced Cubic to Monoclinic Phase Transformation in Erbium Sesquioxide Er₂O₃, *Inorg. Chem.*, 2007, **46**, 6164.
- 10 P. A. Guńka, K. F. Dziubek, A. Gładysiak, M. Dranka, J. Piechota, M. Hanfland, A. Katrusiak and J. Zachara, Compressed Arsenolite As₄O₆ and Its Helium Clathrate As₄O₆-2He, *Cryst. Growth Des.*, 2015, **15**, 3740.
- 11 J. A. Sans, F. J. Manjón, C. Popescu, V. P. Cuenca-Gotor, O. Gomis, A. Muñoz, P. Rodríguez-Hernández, J. Contreras-García, J. Pellicer-Porres, A. L. J. Pereira, D. Santamaría-Pérez and A. Segura, Ordered helium trapping and bonding in compressed arsenolite: Synthesis of As₄O₆-2He, *Phys. Rev. B*, 2016, **93**, 054102.
- 12 V. P. Cuenca-Gotor, O. Gomis, J. A. Sans, F. J. Manjón, A. Muñoz, P. Rodríguez-Hernández and A. Muñoz, Vibrational and elastic properties of As₄O₆ and As₄O₆-2He at high pressures: Study of dynamical and mechanical stability, *J. Appl. Phys.*, 2016, **120**, 155901.
- 13 A. L. J. Pereira, L. Gracia, D. Santamaría-Pérez, R. Vilaplana, F. J. Manjon, D. Errandonea, M. Nalin and A. Beltrán, Structural and vibrational study of cubic Sb₂O₃ under high pressure, *Phys. Rev. B: Condens. Matter Mater. Phys.*, 2012, **85**, 174108.
- 14 Z. Zhao, Q. Zeng, H. Zhang, S. Wang, S. Hirai, Z. Zeng and W. L. Mao, Structural transition and amorphization in compressed α -Sb₂O₃, *Phys. Rev. B: Condens. Matter Mater. Phys.*, 2015, **91**, 184112.

- 15 A. L. J. Pereira, D. Errandonea, A. Beltran, L. Gracia, O. Gomis, J. A. Sans, B. García-Domene, A. Miquel-Veyrat, F. J. Manjon, A. Munoz and C. Popescu, Structural study of α -Bi₂O₃ under pressure, *J. Phys.: Condens. Matter*, 2013, **25**, 475402.
- 16 E. Soignard, S. A. Amin, Q. Mei, C. J. Benmore and J. L. Yarger, High-pressure behaviour of As₂O₃: Amorphous-amorphous and crystalline-amorphous transitions, *Phys. Rev. B: Condens. Matter Mater. Phys.*, 2008, **77**, 144113.
- 17 P. A. Guñka, M. Dranka, M. Hanfland, K. F. Dziubek, A. Katrusiak and J. Zachara, Cascade of High-Pressure Transitions of Claudetite II and the First Polar Phase of Arsenic(III) Oxide, *Cryst. Growth Des.*, 2015, **15**, 3950.
- 18 N. Cornei, N. Tancrét, F. Abraham and O. Mentre, New ϵ -Bi₂O₃ Metastable Polymorph, *Inorg. Chem.*, 2006, **45**, 4886.
- 19 A. L. J. Pereira, J. A. Sans, R. Vilaplana, O. Gomis, F. J. Manjón, P. Rodríguez-Hernández, A. Muñoz, C. Popescu and A. Beltrán, Isostructural Second-Order Phase Transition of β -Bi₂O₃ at High Pressures: An Experimental and Theoretical Study, *J. Phys. Chem. C*, 2014, **118**, 23189.
- 20 N. C. Norman, *Chemistry of arsenic, antimony and bismuth*, Springer, Netherlands, 1998.
- 21 M. Brebu, E. Jakab and Y. Sakata, Effect of flame retardants and Sb₂O₃ synergist on the thermal decomposition of high-impact polystyrene and on its debromination by ammonia treatment, *J. Anal. Appl. Pyrolysis*, 2007, **79**, 346.
- 22 M. M. Si, J. Feng, J. W. Hao, L. S. Xu and J. X. Du, Synergistic flame retardant effects and mechanisms of nano-Sb₂O₃ in combination with aluminum phosphinate in poly (ethylene terephthalate), *Polym. Degrad. Stab.*, 2014, **100**, 70.
- 23 J. H. Youk, R. P. Kambour and W. J. MacKnight, Preparation and Polymerization of Ethylene 2,6-Naphthalenedicarboxylate Cyclic Oligomers, *Macromolecules*, 2000, **33**, 3606–3610.
- 24 G. Venkateshwarlu, K. C. Rajanna and P. K. Saiprakash, Antimony Trioxide as an Efficient Lewis Acid Catalyst for the Synthesis of 5-Substituted 1HTetrazoles, *Synth. Commun.*, 2009, **39**, 426.
- 25 K. E. Alifantis, S. A. Hackney and K. R. Vasant, *High Energy density lithium batteries: materials, engineering, applications*, Wiley VCH, 2010.
- 26 C. M. Park, J. H. Kim, H. Kim and H. J. Sohn, Li-alloy based anode materials for Li secondary batteries, *Chem. Soc. Rev.*, 2010, **39**, 3115.
- 27 J. S. Zabinski, M. S. Donley and N. T. McDevitt, Mechanistic study of the synergism between Sb₂O₃ and MoS₂ lubricant systems using Raman spectroscopy, *Wear*, 1993, **165**, 103.
- 28 A. Ghosh and D. Chakravorty, Transport properties of semi-conducting CuO-Sb₂O₃-P₂O₅ glasses, *J. Phys.: Condens. Matter*, 1991, **3**, 3335.
- 29 L. A. Gómez, C. B. de Araújo, D. N. Messias, L. Misoguti, S. C. Zilio, M. Nalin and Y. Messaddeq, Nonresonant third-order nonlinearity of antimony glasses at telecom wavelengths, *J. Appl. Phys.*, 2006, **100**, 116105.
- 30 R. Koivula, The effect of dopant's valence (+III and +V) on the anion/cation uptake properties of antimony-doped tin dioxide, *Cent. Eur. J. Chem.*, 2010, **8**, 1179.
- 31 K. Samanta, P. Bhattacharya and R. S. Katiyar, Raman scattering studies of p-type Sb-doped ZnO thin films, *J. Appl. Phys.*, 2010, **108**, 113501.
- 32 H. Y. Liu, N. Izyumskaya, V. Avrutin, Ü. Özgür, A. B. Yankovich, A. V. Kvit, P. M. Voyles and H. Morkoc, Donor behaviour of Sb in ZnO, *J. Appl. Phys.*, 2012, **112**, 033706.
- 33 E. Senthil Kumar, F. Mohammadbeigi, S. Alagha, Z. W. Deng, I. P. Anderson, T. Wintchel and S. P. Watkins, Optical evidence for donor behaviour of Sb in ZnO nanowires, *Appl. Phys. Lett.*, 2013, **102**, 132105.
- 34 H. S. Chin, K. Y. Cheong and K. A. Razak, Review on oxides of antimony nanoparticles: synthesis, properties, and applications, *J. Mater. Sci.*, 2010, **45**, 5993.
- 35 A.-H. Geng, L. Cao, C. Wan and Y. Ma, High-pressure Raman investigation of the semiconductor antimony oxide, *Phys. Status Solidi C*, 2011, **8**, 1708.
- 36 A.-H. Geng, L.-H. Cao, Y.-M. Ma, Q.-L. Cui and C.-M. Wan, Experimental Observation of Phase Transition in Sb₂O₃ under High Pressure, *Chin. Phys. Lett.*, 2016, **33**, 097401.
- 37 Y. Zou, W. Zhang, X. Li, M. Ma, X. Li, C.-H. Wang, B. He, S. Wang, Z. Chen, Y. Zhao and B. Li, Pressure-induced anomalies and structural instability in compressed β -Sb₂O₃, *Phys. Chem. Chem. Phys.*, 2018, **20**, 11430.
- 38 L. D. Landau and E. M. Lifshitz, *Statistical physics*, Pergamon Press, London, 1958, ch. 14, p. 430.
- 39 I. M. Lifshitz, Anomalies of Electron Characteristics of a Metal in the High Pressure Region, *Sov. Phys. JETP*, 1960, **11**, 1130.
- 40 P. Ehrenfest, Phase transitions in the usual and generalized sense, classified according to the singularities of the thermodynamic potential, *Proc. R. Acad. Sci. Amsterdam*, 1933, **36**, 153.
- 41 T. E. Jones, M. E. Eberhart and D. P. Clougherty, Topological Catastrophe and Isostructural Phase Transition in Calcium, *Phys. Rev. Lett.*, 2010, **105**, 265702.
- 42 R. J. Angel, J. Gonzalez-Platas and M. Alvaro, EosFit7c and a Fortran module (library) for equation of state calculations, *Z. Kristallogr.*, 2014, **229**, 405–419.
- 43 It must be stressed that the BM EoS order of experimental volume data was determined by the analysis of the F - f plot of theoretical simulations (Fig. S8 (top) in the ESI†). The observation of this plot led us to the first observation of an anomalous compressibility above 10 GPa.
- 44 A. L. J. Pereira, O. Gomis, J. A. Sans, J. Contreras-García, F. J. Manjón, P. Rodríguez-Hernández, A. Muñoz and A. Beltrán, β -Bi₂O₃ under compression: Optical and elastic properties and electron density topology analysis, *Phys. Rev. B*, 2016, **93**, 224111.
- 45 *CrysAlisPRO*, Oxford Diffraction /Agilent Technologies UK Ltd, Yarnton, England.

- 46 G. M. Sheldrick, SHELXT – Integrated space-group and crystalstructure determination, *Acta Crystallogr., Sect. A: Found. Adv.*, 2015, **71**, 3.
- 47 G. M. Sheldrick, Crystal structure refinement with SHELXL, *Acta Crystallogr., Sect. C: Struct. Chem.*, 2015, **71**, 3.
- 48 M. I. Arroyo, J. M. Perez-Mato, C. Capillas, E. Kroumova, S. Ivantchev, G. Madariaga, A. Kirov and H. Wondratschek, Bilbao Crystallographic Server I: Databases and crystallographic computing programs, *Z. Kristallogr.*, 2006, **221**, 15.
- 49 C. A. Cody, L. Dicarlo and R. K. Darlington, Vibrational and thermal study of antimony oxides, *Inorg. Chem.*, 1979, **18**, 1572.
- 50 P. J. Miller and C. A. Cody, Infrared and Raman investigation of vitreous antimony trioxide, *Spectrochim. Acta, Part A*, 1982, **38**, 555.
- 51 A. E. Panasenکو, L. A. Zemnukhova, L. N. Ignatieva, T. A. Kaidalova, S. I. Kuznetsov, N. V. Polyakova and Y. V. Marchenko, Phase composition of antimony(III) oxide samples of different origin, *Inorg. Mater.*, 2009, **45**, 402.
- 52 E. I. Voit, A. E. Panasenکو and L. A. Zemnukhova, Vibrational spectroscopic and quantum chemical study of antimony(III) oxide, *J. Struct. Chem.*, 2009, **50**, 60.
- 53 R. F. W. Bader and M. A. Austen, Properties of atoms in molecules: Atoms under pressure, *J. Chem. Phys.*, 1997, **107**, 4271.
- 54 K. Zhao, Y. Wang, Y. Sui, C. Xin, X. Wang, Y. Wang, Z. Liu and B. Li, First principles study of isostructural phase transition in Sb₂Te₃ under high pressure, *Phys. Status Solidi RRL*, 2015, **9**, 379.
- 55 K. K. Pandey, H. K. Poswal, R. Kumar and S. M. Sharma, High pressure iso-structural phase transition in BiMn₂O₅, *J. Phys.: Condens. Matter*, 2013, **25**, 325401.
- 56 G. Jaegger, The Ehrenfest Classification of Phase Transitions: Introduction and Evolution, *Arch. Hist. Exact Sci.*, 1998, **53**, 51.
- 57 T. Ma and S. Wang, *Phase Transition Dynamics*, Springer, New York Heidelberg Dordrecht London, 2014, 10.1007/978-1-4614-8963-4.
- 58 A. Dewaele, P. Loubeyre and M. Mezouar, Equations of state of six metals above 94 GPa, *Phys. Rev. B: Condens. Matter Mater. Phys.*, 2004, **70**, 094112.
- 59 F. Fauth, I. Peral, C. Popescu and M. Knapp, The new Material Science Powder Diffraction beamline at ALBA Synchrotron, *Powder Diffr.*, 2013, **28**, S360.
- 60 A. P. Hammersley, S. O. Svensson, M. Hanfland, A. N. Fitch and D. Hausermann, Two-dimensional detector software: From real detector to idealised image or two-theta scan, *High Pressure Res.*, 1996, **14**, 235.
- 61 A. C. Larson and R. B. von Dreele, General Structure Analysis System (GSAS), *LANL Report*, 2004, **86**, 748.
- 62 B. H. Toby, EXPGUI, a graphical user interface for GSAS, *J. Appl. Crystallogr.*, 2001, **34**, 210.
- 63 B. Garcia-Domene, H. M. Ortiz, O. Gomis, J. A. Sans, F. J. Manjón, A. Muñoz, P. Rodríguez-Hernández, S. N. Achary, D. Errandonea, D. Martínez-García, A. H. Romero, A. Singhaland and A. K. Tyagi, High-pressure lattice dynamical study of bulk and nanocrystalline In₂O₃, *J. Appl. Phys.*, 2012, **112**, 123511.
- 64 Z. Sui, S. Hu, H. Chen, C. Gao, H. Su, A. Rahman, R. Dai, Z. Wang, X. Zheng and Z. Zhang, Laser effects on phase transition for cubic Sb₂O₃ microcrystals under high pressure, *J. Mater. Chem. C*, 2017, **5**, 5451.
- 65 M. K. Mao, J. Xu and P. M. Bell, Calibration of the ruby pressure gauge to 800 kbar under quasi-hydrostatic conditions, *J. Geophys. Res. Solid Earth*, 1986, **91**, 4673.
- 66 G. J. Piermarini, S. Block and J. D. Barnett, Hydrostatic limits in liquids and solids to 100 kbar, *J. Appl. Phys.*, 1973, **44**, 5377.
- 67 S. Klotz, J.-C. Chervin, P. Munsch and G. Le Marchand, Hydrostatic limits of 11 pressure transmitting media, *J. Phys. D: Appl. Phys.*, 2009, **42**, 075413.
- 68 P. Hohenberg and W. Kohn, Inhomogeneous Electron Gas, *Phys. Rev.*, 1964, **136**, B864.
- 69 G. Kresse and J. Hafner, Ab initio molecular dynamics for liquid metals, *Phys. Rev. B: Condens. Matter Mater. Phys.*, 1993, **47**, 558.
- 70 G. Kresse and J. Furthmüller, Efficiency of ab-initio total energy calculations for metals and semiconductors using a plane-wave basis set, *Comput. Mater. Sci.*, 1996, **6**, 15.
- 71 G. Kresse and J. Furthmüller, Efficient iterative schemes for ab initio total-energy calculations using a plane-wave basis set, *Phys. Rev. B: Condens. Matter Mater. Phys.*, 1996, **54**, 11169.
- 72 P. E. Blöchl, Projector augmented-wave method, *Phys. Rev. B: Condens. Matter Mater. Phys.*, 1994, **50**, 17953.
- 73 G. Kresse and D. Joubert, From ultrasoft pseudopotentials to the projector augmented-wave method, *Phys. Rev. B: Condens. Matter Mater. Phys.*, 1999, **59**, 1758.
- 74 J. P. Perdew, A. Ruzsinszky, G. I. Csonka, O. A. Vydrov, G. E. Scuseria, L. A. Constantin, X. Zhou and K. Burke, Restoring the Density-Gradient Expansion for Exchange in Solids and Surfaces, *Phys. Rev. Lett.*, 2008, **100**, 136406.
- 75 K. Momma and F. Izumi, VESTA|3 for three-dimensional visualization of crystal, volumetric and morphology data, *J. Appl. Crystallogr.*, 2011, **44**, 1272.
- 76 K. Parlinsky, *Computer code PHONON*, 2008. URL: wolf.ifj.edu.pl/phonon/.